LABORATORI NAZIONALI DI FRASCATI
SIS-Pubblicazioni

LNF-01/016(P)
23 Aprile 2001

The Tracking Detector of the KLOE Experiment

The KLOE Collaboration*

Abstract

The design and construction of the large Drift Chamber for the KLOE experiment at the Frascati ϕ–factory, DAΦNE, are described. The relevant aspects of the various elements of the detector are reviewed together with a description of the track reconstruction program and of the calibration procedures. The performance of the detector based on measurements with cosmic rays and with e^+e^- colliding beams during DAΦNE commissioning is presented.

PACS:29.40.Cs

Submitted to Elsevier for pubblication on Nucl. Instrum. Meth. A.

*The KLOE Collaboration:
M. Adinolfi,[a] F. Ambrosino,[b] A. Andryakov,[c,m], A. Antonelli,[c] M. Antonelli,[c] C. Bacci,[d] R. Baldini-Ferroli,[c] A. Bankamp,[e] F. Bellini,[d] G. Bencivenni,[c] S. Bertolucci,[c] C. Bini,[f] C. Bloise,[c] V. Bocci,[f] F. Bossi,[c] P. Branchini,[d,‡], S. A. Bulychjov,[m] G. Cabibbo,[f] A. Calcaterra,[c] R. Caloi,[f] P. Campana,[c] G. Capon,[c] A. Cardini,[f] M. Casarsa,[g] V. Casavola,[h] G. Cataldi,[h,†], F. Ceradini,[d] F. Cervelli,[i] G. Chiefari,[b] P. Ciambrone,[c] E. De Lucia,[f] R. De Sangro,[c] P. De Simone,[c] S. Dell'Agnello,[c] A. Denig,[e,†], A. Di Domenico,[f] C. Di Donato,[b] S. Di Falco,[i] A. Doria,[b] E. Drago,[b] G. Felici,[c] A. Ferrari,[d] M. L. Ferrer,[c] G. Finocchiaro,[c] G. Fischer,[e] C. Forti,[c] A. Franceschi,[c] P. Franzini,[f,j], C. Gatti,[c] P. Gauzzi,[f] S. Giovannella,[c] V. Golovatyuk,[h] E. Gorini,[h] F. Grancagnolo,[h] E. Graziani,[d,‡], M. Incagli,[i] L. Ingrosso,[c] Y. Y. Jiang,[c,n], W. Kluge,[e] V. Kulikov,[m] C. Kuo,[e] F. Lacava,[f] G. Lanfranchi,[c] J. Lee-Franzini,[c,k], T. Lomtadze,[i] C. Luisi,[f] M. Martemianov,[c,m], M. Matsyuk,[c,m], W. Mei,[c] A. Menicucci,[a] R. Messi,[a] S. Moccia,[c] M. Moulson,[c] S. Müller,[e] F. Murtas,[c] M. Napolitano,[b] A. Nedosekin,[c,m], L. Pacciani,[a] P. Pagès,[c] M. Palutan,[d] M. Panareo,[h] L. Paoluzi,[a] E. Pasqualucci,[f] L. Passalacqua,[c] M. Passaseo,[f] A. Passeri,[d,‡], V. Patera,[c,l], E. Petrolo,[f] G. Petrucci,[c] D. Picca,[f] M. Piccolo,[c] G. Pirozzi,[b] M. Pollack,[k] L. Pontecorvo,[f] M. Primavera,[h] E. Santovetti,[a] G. Saracino,[b] F. Schönleber,[e] B. Sciascia,[f] A. Sciubba,[c,l], I. Sfiligoi,[c] T. Spadaro,[f] S. Spagnolo,[h] E. Spiriti,[d,‡], U. von Hagel,[e] P. Valente[c1], B. Valeriani,[e] G. Venanzoni,[j,†], S. Veneziano,[f] A. Ventura[h]

[a] Dipartimento di Fisica dell'Università "Tor Vergata" e Sezione INFN Roma II, Roma, Italy.
[b] Dipartimento di Scienze Fisiche dell'Università e Sezione INFN, Napoli, Italy.
[c] Laboratori Nazionali di Frascati dell'INFN, Frascati, Italy.
[d] Dipartimento di Fisica dell'Università "Roma Tre" e Sezione INFN Roma III, Roma, Italy.
[e] Institut für Experimentelle Kernphysik, Universität Karlsruhe, Germany.
[f] Dipartimento di Fisica dell'Università "La Sapienza" e Sezione INFN Roma, Roma, Italy.
[g] Dipartimento di Fisica dell'Università e Sezione INFN, Trieste, Italy.
[h] Dipartimento di Fisica dell'Università e Sezione INFN, Lecce, Italy.
[i] Dipartimento di Fisica dell'Università e Sezione INFN, Pisa, Italy.
[j] Physics Department, Columbia University, New York, USA.
[k] Physics Department, State University of New York at Stony Brook, USA.
[l] Dipartimento di Energetica dell'Università "La Sapienza", Roma , Italy.
[m] Permanent address: Institute for Theoretical and Experimental Physics, Moscow, Russia.
[n] Permanent address: Institute of High Energy Physics of Academica Sinica, Beijing, China.
† formerly Institut für Experimentelle Kernphysik, Universität Karlsruhe, Germany.
‡ formerly Sezione INFN Istituto Superiore di Sanità, Roma, Italy.

[1] corresponding author

1 Introduction

The main goal of the KLOE experiment [1] at the Frascati ϕ–factory, DAΦNE, is the precise measurement of the CP-symmetry violation parameters in the decay of neutral kaons. DAΦNE [2] is a double-ring e^+e^- collider designed to attain a peak luminosity of 5×10^{32} cm^{-2} s^{-1} with 120 bunches and a crossing period of 2.7 ns. The beams cross at an angle of 25 mrad and ϕ-mesons are produced with a small transverse momentum of 13 MeV/c and a cross section of $\sim$3 μb. Neutral kaons are coherently produced through the decay $\phi \to K_S K_L$ and the study of the decay products with large statistics offers a unique opportunity to do a number of tests of CP and CPT invariance by studying the time evolution of different final states [3]. Kaon

Decay	Momentum MeV/c	Decay length cm
$\phi \to K^+K^-$	p_K=127	$\lambda^{\pm}$=95
$\phi \to K_S K_L$	p_K=110	λ_L=343, λ_S=0.59
K_L– K_S	155< p_π <265	–

Table 1: Kinematics of decays at DAΦNE.

pairs are produced at large polar angles relative to the beam axis: $\mathrm{d}\sigma/\mathrm{d}\cos\theta \sim \sin^2\theta$. The relevant features of the decays are listed in tab. 1. The design of the experiment is driven by the requirements of a large acceptance for K_L decays into charged and neutral particles, precise location of the decay vertices, good invariant mass resolution, γ–e–π identification and good self-calibrating capabilities. The cross section of the KLOE detector is shown in fig. 1.

The decay volume around the interaction point – 2 m in radius and 3.3 m in length – is occupied by a large tracking chamber surrounded by a hermetic calorimeter [1,4] to measure the energy and impact point of photons. Its large dimensions are forced by the long K_L mean decay path at DAΦNE. The tracking chamber and the calorimeter are immersed in the magnetic field of a superconducting coil of 2.5 m inner radius and 4.2 m length. The value of the magnetic field, 0.6 T, has been chosen to optimize the acceptances, pattern recognition and momentum resolution. The low-β quadrupoles are located between the vacuum pipe and the tracking chamber on both sides of the interaction point. Here the beam pipe is made of Al-Be alloy, 0.5 mm thick, to minimize the energy loss of charged particles, and has a spherical shape with 10 cm radius so that all K_S mesons decay in vacuum.

The design of the tracking detector [5] is driven by the requirements of having a large, highly homogeneous active volume enclosed by low-mass walls to minimize K_L regeneration (which might simulate CP-violating decays), multiple scattering and photon absorption. The active volume has low Z and density. The detector provides tracking in three dimensions with a resolution in the bending plane of $\sim$200 μm and a decay vertex resolution of $\sim$ 1 mm over the whole sensitive volume. It also provides a fast trigger for charged particles to complement the trigger of the calorimeter.

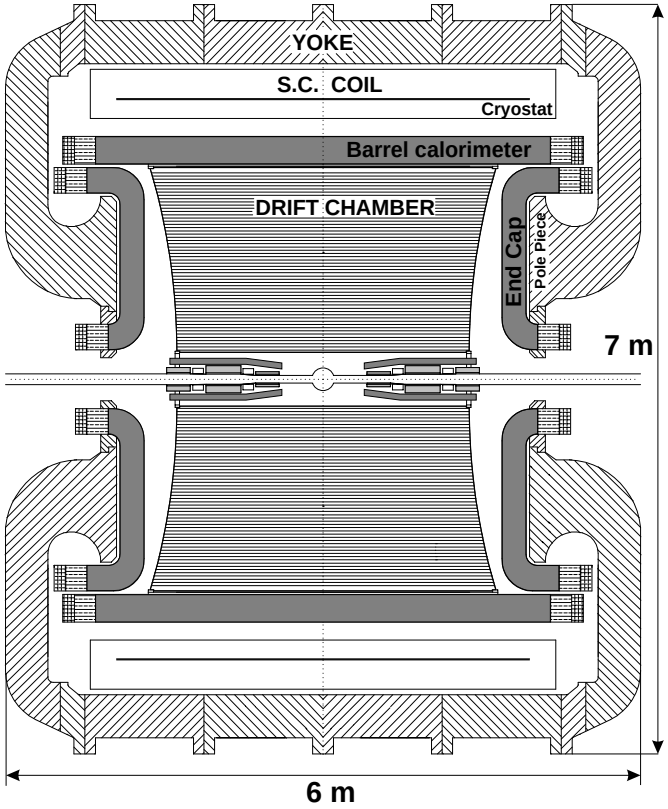

Figure 1: Vertical cross section of the KLOE detector along the beam line.

The solution that meets the above requirements is a cylindrical drift chamber whose structure is entirely made of carbon fibers and a light gas mixture, 90% He–10% iC$_4$H$_{10}$. The electric field configuration, mechanical structure, choice of materials, construction technique, front-end electronics and read-out are described in the following sections as well as the results of the operation with cosmic rays and during the first runs of data taking at DAΦNE in 1999.

2 Design considerations

2.1 Drift cell

The requirements of three-dimensional track reconstruction and of uniform efficiency throughout the chamber volume led to the choice of drift cells of almost square shape arranged in coaxial layers with alternating stereo angles. The stereo angle of the $k^{\rm th}$ layer, ε_k, is the angle between the wires and the chamber axis. As shown in fig. 2, the radial distance of a wire from the chamber axis varies along the longitudinal direction, z, being maximum at the end-plates, R_k, and minimum at the center, R_{k0}. The most uniform filling of the sensitive volume is obtained by choosing a constant value for the difference $\delta_k = R_k - R_{k_0}$ [6]. The

relation between the stereo angle and δ is

$$\tan\varepsilon_k = \pm\frac{2\delta}{L_k}\sqrt{\frac{2R_{k_0}}{\delta} - 1}$$

where L_k is the distance between the chamber end-plates for the wires of the k^{th} layer. The requirement of good resolution in the measurement of the z coordinate, $\sigma_z = \sigma_{r\phi}/\tan\varepsilon$, together with that of a reasonably small stereo angle led to the choice of $\delta = 1.5$ cm. Thus the stereo angle increases with the radius from $\pm$ 60 mrad to $\pm$ 150 mrad. With an average $r\phi$ resolution of 200 μm, the z resolution is about 2 mm over the whole chamber volume. In this "all-stereo" configuration, the shape of an almost-square drift cell changes

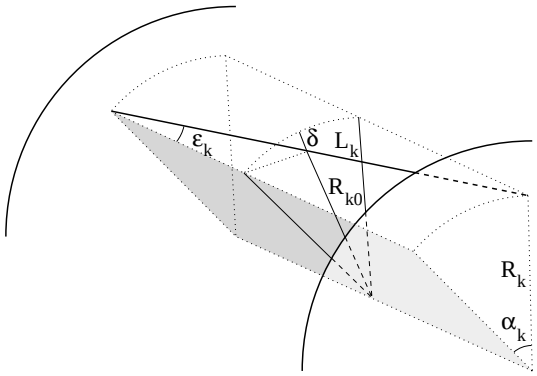

Figure 2: Wire geometry. ε_k is the stereo angle and α_k the difference in azimuth at the two ends for a wire in the $k^{\rm th}$ layer. R_{k0} and R_k are the wire radius at z=0 and at the endplates. The decrease in radius, δ=1.5 cm at the chamber center, is also shown.

slowly along z in a periodic way. Uniformity of response is obtained if the variations of the electric field are kept small with a number of field shaping wires that close the drift cell. Detailed studies of the field configuration performed with accurate simulation codes [7] and on prototypes [8] have shown that a ratio of field to sense wires of 3:1 is a satisfactory solution that ensures good electrostatic properties of the drift cell while still maintaining an acceptable track sampling frequency.

The drift cell configuration is shown in fig. 3: the field wire at radius R_{k-1} and the sense wire at R_k are parallel with almost the same stereo angle, $\varepsilon_{k-1} \approx \varepsilon_k$, while the field wires at radius R_{k+1} are shared with the next layer of drift cells and have opposite stereo angle, $\varepsilon_{k+1} \approx -\varepsilon_k$. The number of drift cells in a layer, N_k, must be an integer. If $w = R\Delta\phi$ is the width of a cell and $h = \Delta R$ is its half-height, in order to always use the same periodicity in high voltage and signal connections the increment $\Delta N = N_{k+1} - N_k$ must be a constant

$$N_k = 2\pi R_k/w \qquad \Delta N = N_{k+1} - N_k = 2\pi h/w = \text{const.}$$

Several measurements on prototypes with low- and high-energy particle beams, with and without magnetic field have shown that the design performance can be met with drift cells of ~ 3 cm width. Since the track density is much higher at small radii due to the small momenta of charged particles produced in ϕ decays,

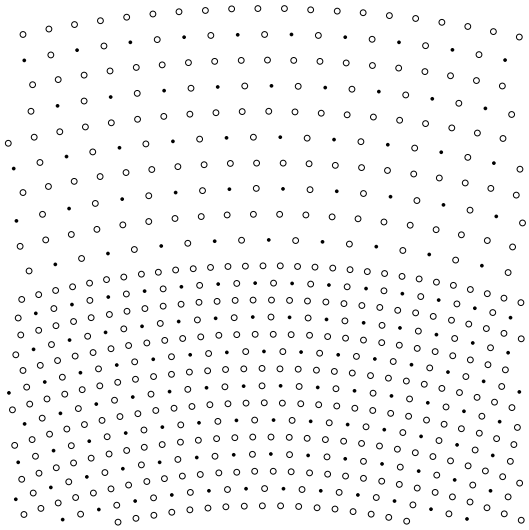

Figure 3: Drift cells configuration at z=0: a portion of chamber at the boundary between small cells (inner layers) and big cells (outer layers) is shown. Full dots indicate sense wires, open circles the field wires.

and since vertexing of $K_S \to \pi^+\pi^-$ decays is required, the innermost layers have cells of smaller size. The choice was

$h = 2$ cm $\quad w = 2\pi/3$ cm $\quad \Delta N = 6 \quad$ for the 12 innermost layers

$h = 3$ cm $\quad w = 3\pi/3$ cm $\quad \Delta N = 6 \quad$ for all other layers

Simulation studies, confirmed by the results of tests with prototypes, have shown that good efficiency and spatial resolution and safe operation conditions in terms of aging in the DAΦNE radiation environment are obtained using a helium-based gas mixture with a gas gain of $\sim 10^5$. With the adopted drift-cell geometry this requirement is met with sense wires of 25 μm and field shaping wires of 80 μm diameter at a voltage difference of $1800 - 2000$ V. With these choices, and a magnetic field of 0.6 T, we obtain the drift line configurations shown in fig. 4 for the average shape of a small and a big drift cell.

The chamber volume is enclosed by two cylindrical walls at radii of 25 cm and 194 cm and two end-plates at a maximum $L = 330$ cm. The number of layers is 58: 12 layers consist of *small cells* at radii R=28.5–52.5 cm and 46 layers consist of *big cells* at radii R=52.5–190.5 cm. The number of drift cells per layer increases by $\Delta N = 6$ from one layer to the next, except at the boundary between small and big cells where $\Delta N = -42$. Two layers of guard field-shaping wires are located at radii $R_{in} = 27.5$ cm and $R_{out} = 191.5$ cm. The wire spacing for the inner (outer) layer of guard wires is 1.0 cm (1.5 cm). The number of drift cells is 12,582 and the total number of sense and field shaping wires is 52,140.

2.2 Gas mixture

A helium-based gas mixture was chosen to minimize multiple scattering and density. The relevant properties of the gas mixture, either measured directly [9,10,13], or computed with transport equations [14,15], are listed in tab. 2. The drift velocity as a function of the electric field is shown in fig. 5 where our measurement

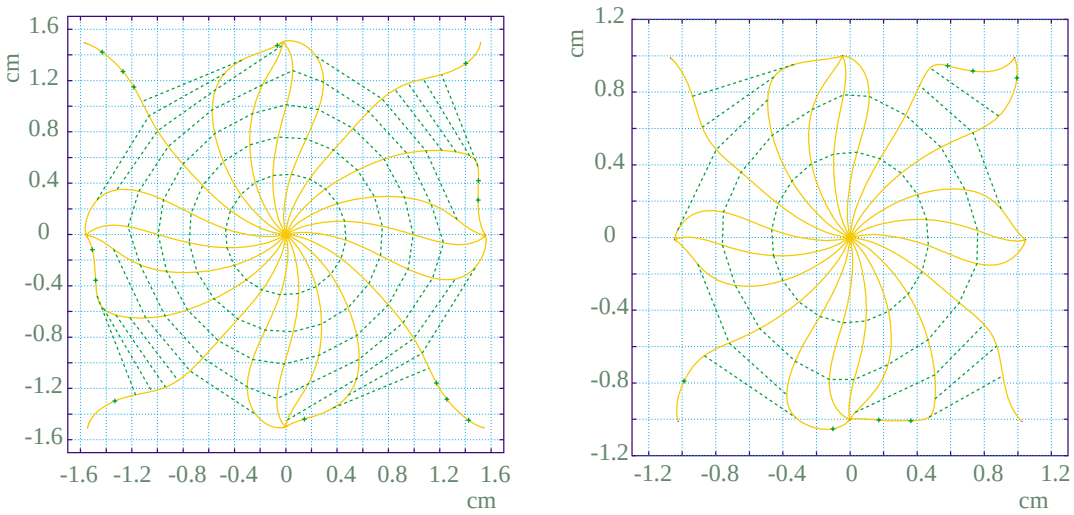

Figure 4: Example of the drift lines for a big (left) and a small (right) cell.

[9] is compared to other measurements and calculations.

Parameter	Value	Ref.
N. primary clusters[1]	12.3±0.2 cm^{-1}	[9,10]
Total specific ionization[1]	∼9 cm^{-1}	[10]
Drift velocity, E= 0.5–1 kV/cm	17–23 mm/μs	[9]
Drift angle, E= 0.5–1 kV/cm	0.2–0.3 rad	[9,14]
Diffusion coeff., E= 0.5–1 kV/cm	(3.2–2.5)×10^{-4} $cm^2/\mu s$	[13]
Radiation length	∼1300 m	

Table 2: Properties of the 90% He - 10% iC_4H_{10} gas mixture.

Most of these measurements were performed with small-size prototypes and no stereo geometry. A full-length prototype [16] that reproduces a wedge of the tracking detector was built to test the materials, the construction technique and the front-end electronics and to assess whether the all-stereo wire geometry would meet the design performance. Measurements with a particle beam have proven the self-calibration capability of the detector and that an average spatial resolution of 130 μm can be attained for high momentum particles.

[1]For a minimum ionizing particle

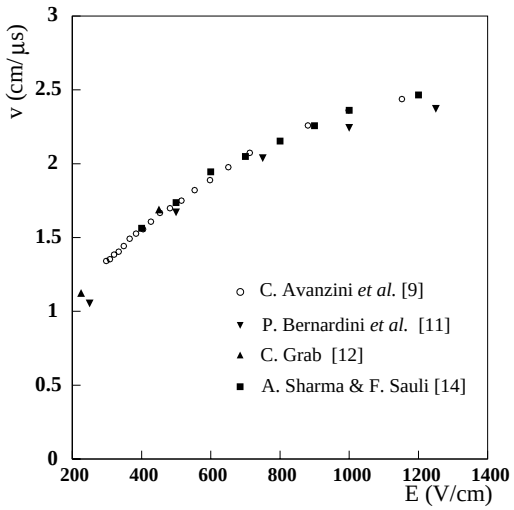

Figure 5: Drift velocity as a function of the electric field.

3 Mechanical structure

The cylindrical chamber structure is completely made of carbon fiber composite; some dimensions and properties are given in tab. 3. Both ends of the cylinder are closed by two end-plates shaped as spherical caps (at 9.76 m radius) with a 25 cm radius hole in the center. The deviation from the spherical shape was measured to be less than 1 mm. The end-plates are kept apart by twelve struts attached to the L-shaped outer rims of the plates (see fig. 6). Because of the large size of the end-plates, it was necessary to fabricate them in two halves. The half plates were separately cured and then glued together. 52140 holes are drilled in each end-plate for the insertion of feedthroughs. Hole positions are accurate at the level of 60 μm as verified by videogrammetry. The Young modulus loss after the drilling was measured to be about 10%.

The total axial load on the end-plates, about 3500 kg, would deform the end-plates by several mm after the stringing. The problem of the deformation due to wire tension was solved by using rings of rectangular cross section which surround the L-shaped plate rims, made of the same material. The ring is used to apply a tangential pull to the spherical plate via 48 tensioning screws made of titanium alloy pulling on tapped aluminum inserts in the L-shaped flange, as seen in fig. 6. The net result of the pull is to approximate a complete sphere beyond outer edge of the plate which greatly reduces the deformation [17], as shown in fig. 7. Each screw was instrumented with two strain gauges, calibrated in order to compensate for bending effects on the screws, so that the pulling force was always known.

The outer cylindrical wall is composed of twelve panels each made of a sandwich of two layers of 1.5 mm intermediate modulus carbon fiber fabric[2] glued on 3.6 cm of honeycomb. The 12 struts have a hollow rectangular section of 5×3 cm^2 and 0.5 cm thickness. Since they work under compression and see a bending moment at the ends due to the wire load, they were designed to avoid buckling instability. They

[2]Vicotex 1454N/G950

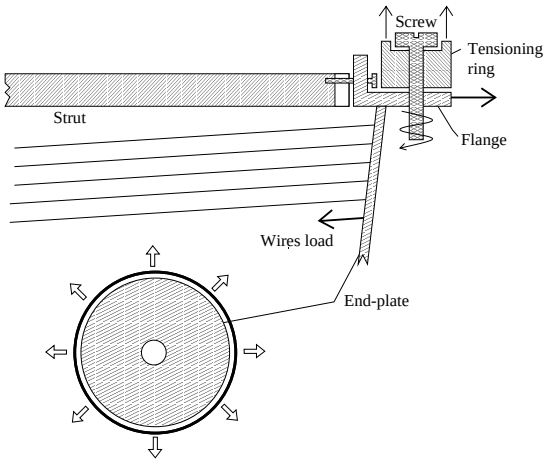

Figure 6: Tensioning ring principle.

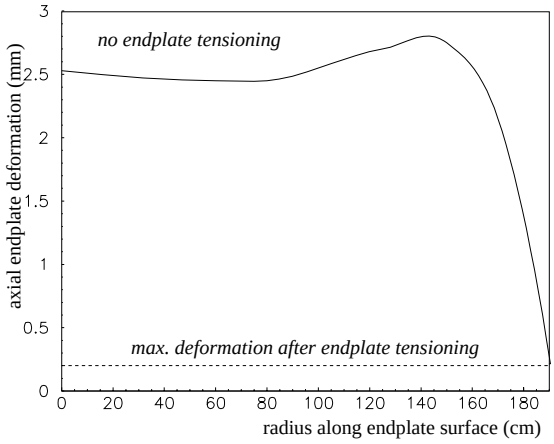

Figure 7: Finite element calculation of endplate deformation.

Outer radius	1980 mm
Outer panels thichkness	39.0 mm
Inner cylinder radius	250 mm
Inner cylinder thickness	1.1 mm
End-plate radius of curvature	9760 mm
End-plate thickness	9 mm (0.03 X_0)
C-fiber X_0	26.7 cm
Maximum length	3320 mm
Minimum length	2800 mm
Number of drift cells	12,582
Number of wires	52,140
End-plate wire load	3500 kg

Table 3: Mechanical and construction characteristics.

were laminated around a fixture with a unidirectional high modulus tape.[3] The inner cylinder is made of a 0.75 mm thick tape of the same unidirectional high modulus carbon fiber and is aluminated on both sides with a foil of 0.10 mm.

The outer panels and the inner cylinder were glued after installing and tensioning the wires so that the panels provide the gas sealing and the necessary bending and torsional stiffness while the inner cylinder has only sealing purposes.

4 Wires and feedthroughs

Gold plated 25 μm diameter tungsten wires are used as anodes. The chamber gas has a radiation length X_0 $\sim$1300 m. The W wires lower the average value of the radiation length in the chamber volume to $\sim$900 m.

Aluminum is a natural choice for the field wires because of low Z and low density, which also results in a smaller load on the end-plates. Silver-plated 5056-Al tempered alloy wire [18] was chosen with a diameter of 80 μm to limit field emission and gas amplification near the field wire surface [19]. Aging tests performed on a small single-cell prototype irradiated with X-rays showed a gain loss of less than 5% after collecting a charge of about 3 mC/cm [20]. The charge collected by the innermost layers during operation with colliding beams in 1999 is estimated to be about 1 mC/cm. Wire properties are given in tab. 4.

In order to mantain equal sag for W and Al wires, the creep of aluminum must be taken into account. Creep is a long term plastic deformation which depends on the alloy and the manufacturing process. A creep test was performed on several Al wires suspended with different loads [21]. A wire elongation of

[3] Vicotex NCHM 174B110/M55J

Wire material	Sense W+Au	Field Al5056+Ag
Diameter (μm)	25.0	81.4
Coating diameter (μm)	0.25	1.0
Linear density (mg/m)	9.3	16.5
X_0 (cm)	0.35	8.9
Elastic limit (g)	$\sim$100	$\sim$350
Ultimate tensile strength (g)	$\sim$160	$\sim$410

Table 4: Wire properties.

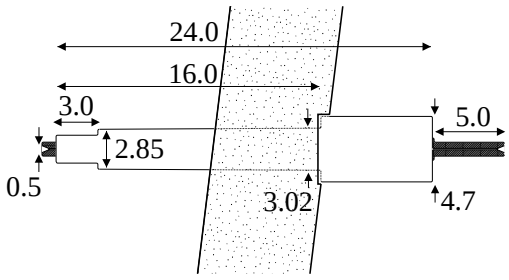

Figure 8: Details of the feedthrough shown inserted in the chamber endplate (dimensions in mm).

$\sim$1.5 mm was measured over 1.5 years for 1.7 m long wires at a temperature of 21 °. This corresponds to a tension loss of $\sim$10 g for a chamber wire.

Wire-crimping is the standard choice for wire clamping. With aluminum, the proper choice of feedthrough material is important. The metal pins, made of copper, are fabricated by precision machining of short sections from drawn tubes. The outer diameter of the pin is 1 mm and the internal hole is 150 μm. The insulating bushing, made of delrin, is injection molded over the metallic pin, to insure a good gas tightness. The same feedthrough, fig. 8, is used to hold both W and Al wires and provides a wire location accuracy of $\leq$30 μm. A reliable crimping is obtained with a pneumatic tool with cylindrical jaws and a carefully adjusted residual gap.

5 Chamber stringing

A semi-automatic system [22,23] was realized in order to support the chamber structure, rotate it to any azimuthal angle, pull wires between the *correct* holes in the end-plates, stretch the wires to the appropriate mechanical tension and crimp the feedthroughs. The insertion of the wire into the feedthrough and of the

feedthrough into the end-plate were performed manually by two operators. Stringing was carried out in a clean room, of class 1000 in the area of the drift chamber and class 10000 in the working area. The temperature of the clean room was held to within $\pm 1\,^{\circ}$C to avoid thermal cycling of the wires.

The whole chamber structure was supported by a steel shaft mounted on a rigid structure with end platforms for operators. The two end-plates were attached to steel collars, one rigidly connected to the shaft and one connected via a linear bearing allowing only axial motion. The shaft was positioned by the control program to an accuracy of 200 μm at the outer rim of the end-plates, at a radius r=2 m.

The wire transport from one end-plate to the other was performed by a robot capable of moving along the x, y and z direction (see fig. 9). A long arm moves on rails longitudinally (along z) and radially (along x) towards the center and outside of the chamber. This arm carries a smaller arm with vertical motion, along y, equipped with a wire carrying tool, called the "nose", which can reach all the holes in the end-plates. All movements were controlled to an accuracy of 0.5 mm.

Crimping of the feedthroughs was done with gas-operated tools mounted on the head of two external robots which also carry the wire spools and the tensioning servos. Both heads could move along three axes and were computer controlled. The position of the crimping tool was controlled to better than 0.5 mm to guarantee a well centered crimp and avoid pin bending. Wire tensioning was computer controlled using a signal from a torquemeter.

A schematic view of the stringing system is shown in fig. 9 as seen from one end-plate, and shows the system for the chamber rotation, one of the two platforms on which operators perform the two manual operations mentioned and the wire carrying robot.

End-plate deformation recovery with the tensioning screws was performed after every 400 kg of additional wire load. Deformations and recovery were determined by measuring the mechanical tension of a sample of wires on different layers.

All robot movements were driven by commercial programmable servo-controllers, connected by serial ports to a computer. The stringing program was developed using commercial programming tools. [4] Skilled operators could safely string a wire in 1.5 minutes. Stringing shifts covered 17 out of 24 hours with three alternating crews of two operators on the end stations and a shift supervisor, who controlled the stringing program and all of the automatic or semi-automatic systems. The night hours were used for system upgrades and debugging, and for quality control measurements. The stringing of the whole chamber took 11 months. Fig. 10 shows the drift chamber in the clean room at the end of wire stringing.

6 Survey and alignment

Due to the very light structure of the chamber particular care was devoted to alignment and survey [24].

The coordinate system of each plate is defined by 12 holes of 6 mm diameter: 4 axial holes on the outer flange, 4 axial holes on the inner flange, plus 4 radial holes on the outer flange. In addition, 54

[4] National Instruments *LabVIEW*™.

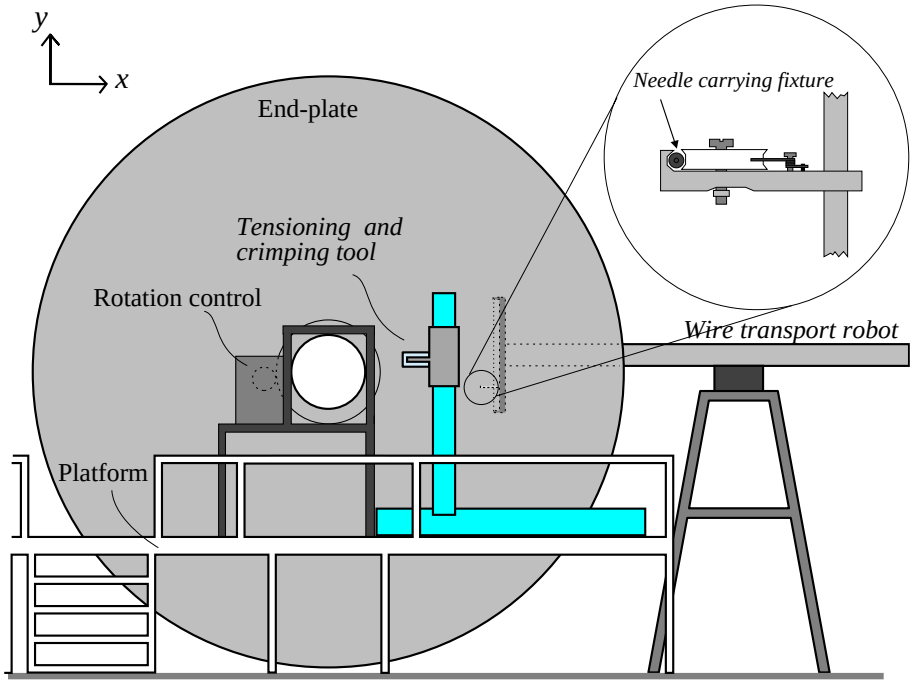

Figure 9: Sketch of the stringing system as seen from one end-plate. The wire transport robot is shown partially inserted into the chamber. Details of the needle carrying extension or "nose" are also shown.

holes were drilled uniformly scattered on the end-plate surface. These 66 reference holes and a sample of 250 wire holes were surveyed by videogrammetry with an accuracy of 25 μm in x and y (transverse plane). After applying the relevant corrections, the final error on the wire positions is 60 μm in the transverse plane.

The common axis of the shaft carrying the chamber and of the end-plates is the chamber z-axis. By means of a level (20 μm accuracy up to 50 m distances) and geodetic targets on the reference holes, the x, y axes were aligned in azimuth and the z axis was set horizontal. The chamber y axis was taken vertically upward, and the origin was chosen as the geometric center of the chamber.

The reference holes were used to survey the chamber and to measure possible deformations during stringing and installation. A high resolution theodolite with an infrared distancemeter was employed. The instrument was connected to a portable PC, allowing quasi real-time measurements. Typical accuracy was 10 μrad for angles and 100 μm for distances. The end-plates were often checked for:

- parallelism and position of the reference holes, indicating that structural deformations were negligible;
- constancy of the relative ϕ angle, of 0.4$\pm$ 0.1 mrad;
- relative x-y shifts of the coordinate systems of the two end-plates found to be 2.0 $\pm$ 0.3 mm during stringing (maximum value) and 1.2 $\pm$ 0.3 mm after installation;
- the relative distance between the end-plates, to an accuracy better than 1 mm.

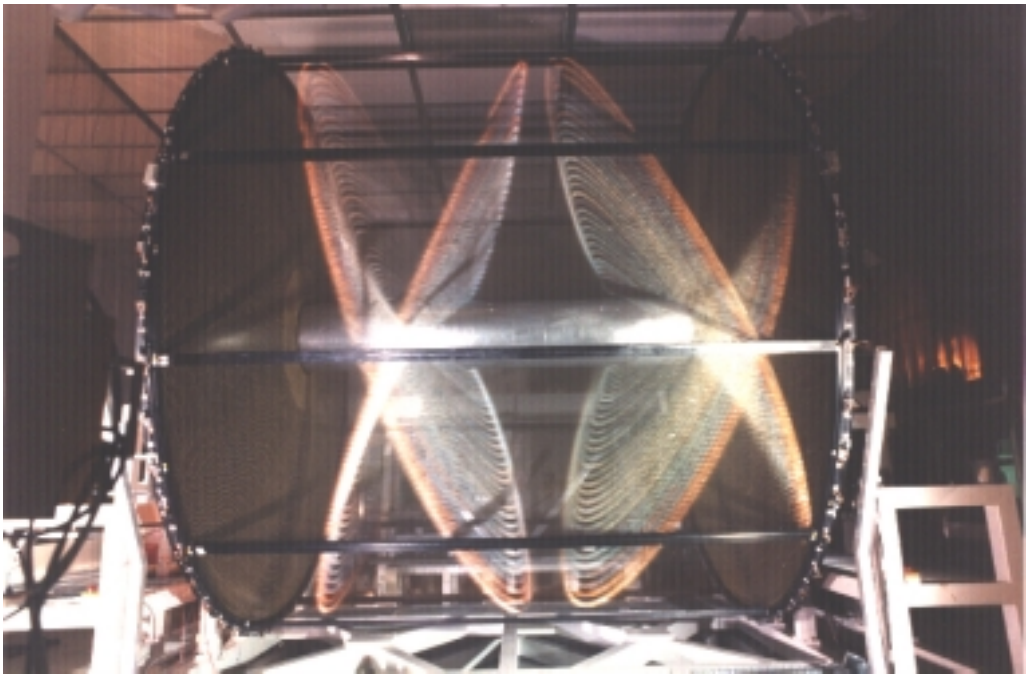

Figure 10: Photograph of the 52,140 wires strung in the chamber.

The stringing robots were also surveyed, both for movement accuracy and position with respect to the chamber, to an overall accuracy of 0.5 mm.

7 Quality tests

Upon completion of each layer and/or in parallel with stringing measurements, quality tests were performed to check electrical behaviour and tensioning of all wires. Wire quality and electrical insulation were tested by applying 3 kV for about 1 minute. Wires were accepted if they drew less than 1 μA in air. Air humidity is critical for this measurement. The relative humidity in the clean room was kept at a constant value of 50%. About 2% of the wires failed the test and were replaced.

The mechanical tension of each wire was determined by measuring the wire resonance frequency with electrostatic excitation and sensing [25]. This method allows measuring the wire tension of any wire at any time. It was used to monitor the tension on a sample of wires during the various phases of stringing, assembly, transport and installation of the drift chamber. Oscillation is induced applying a 1.4 kV signal to the wire. The resonance frequency, f, is extracted by fitting the excitation curve. The wire tension T (in grams), is given by $T = 4f^2\ell^2\mu/g$ where ℓ is the wire length, μ its linear density and g is the gravitational acceleration. The gravitational sag at the center s is found from $s = \mu\ell^2/8T = g/32f^2$. The accuracy of the method was about 1%.

A wire was accepted if the tension was within $\pm 10\%$ of the nominal value. 0.9% of the wires were replaced. Fig. 11 shows the sag distribution immediately after the completion of each layer (top) and at the

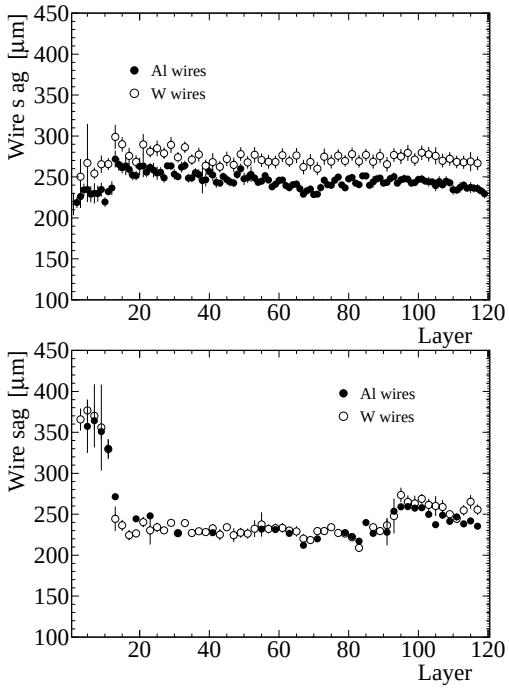

Figure 11: Wire sags for Al and W wires immediately after the completion of each layer, top, and at the end of the stringing, bottom (see text).

end of stringing (bottom). The first 11 layers were strung with the inner flanges of the endplates axially locked. The endplates were then freed resulting in a loss of tension. The inner wires have a sag 100 μm larger than the nominal value of 250 μm. This is corrected for in track recostruction.

8 Gas system

The choice of helium introduces several complications

- the drift velocity is not saturated thus requiring tight control of the gas mixture
- He leaks more rapidly than any other gas
- He is relatively expensive and the chamber is large

Stainless steel components are used throughout and the mixture parameters are continuously monitored [26]. Pressure is also controlled and monitored since the chamber must not see an overpressure exceeding a few millibars, which would result in stretching of the wires, before reaching safety limits. The system is computer operated. All sensors are read into a computer which operates the system controls. Full error handling and data archiving is incorporated. Comnunication with the slow control system is also provided for operator monitoring.

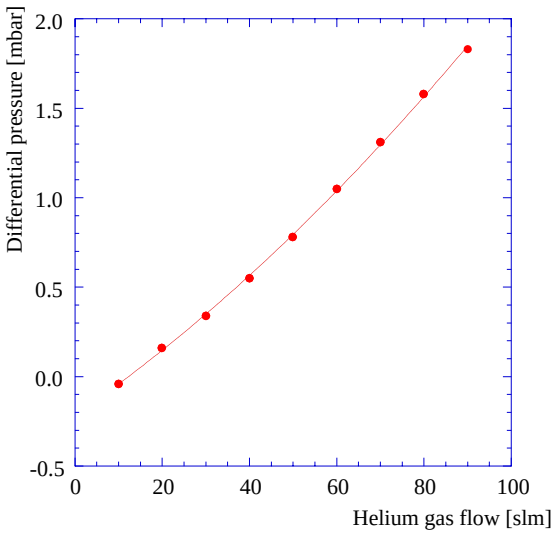

Figure 12: Differential pressure as a function of the gas flow rate in the open mode.

The gas system can operate either in open or closed mode. In closed mode the gas is circulated by means of a metal bellows pump. Typical gas flow is 30 slm[5] corresponding to about 1 volume change per day. Purification of the mixture is necessary due to gas leaks. In open mode the system can provide high gas flows up to 100 slm for the initial flushing of the chamber. The oxygen concentration in open mode depends on the gas flow; for 7.5-30 slm the O_2 contamination is in the range 40-100 ppm. No significant decrease of efficiency has been observed for values larger than 200 ppm. Only the open mode is used because of the excellent gas tightness of the chamber. Figure 12 shows the differential pressure as a function of gas flow. The force on the end-plates at an overpressure of 2.0 mbar results in an elongation of the wires of about 100 μm. Dependence of wire elongation on gas overpressure is shown in fig. 13. In closed mode, any differential pressure below 2 mbar can be used, compensating for variations of the atmospheric pressure to keep the overpressure constant. The closed mode was tested successfully for a period of one week.

The gas system guarantees the following operation limits:

- differential pressure to ± 0.1 mbar;
- isobutane concentration to $\pm 0.06\%$

When flushing in open mode with constant gas flow the oxygen partial pressure reaches a plateau within a few days. From the time necessary to reach equlibrium with different gas flow rates it is possible evaluate the leak rate of the whole system. An increase of the leak rate is observed when the overpressure decreases.

In closed mode *without* purification the oxygen content increases linearly due to chamber leaks. The slope determines the leak rate. Both methods gave similar results for the leak rate. The average value is 5×10^{-2} mbar l s^{-1} at an overpressure of 0.5 mbar. This corresponds to a total flow of oxygen *into* the drift

[5] standard liters per minute

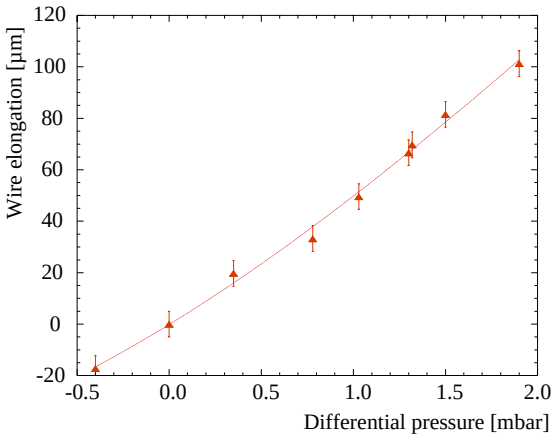

Figure 13: Wire elongation as a function of the differential pressure.

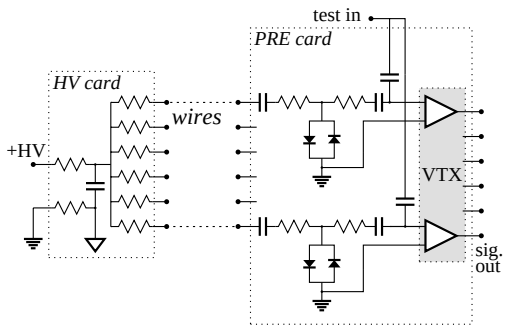

Figure 14: Wire connections to high voltage supply and preamplifiers.

chamber of less than 1 liter/day. If there is no overpressure in the chamber, or a small underpressure, this flow becomes larger than 9 l/d. Therefore, a bubbler was installed at the outlet of the chamber which allows the choice of an arbitrary differential pressure (*i.e.* a leakage rate) at any gas flow; the chamber is normally operated at 0.5-1 mbar of overpressure at a flow of 7.5 slm, which ensures oxygen and water content below 100 ppm.

9 High voltage distribution, front-end electronics and read-out

Good performance of the chamber requires full efficiency for single electron primary clusters, which is necessary to obtain good space resolution with a low density gas. The electronic processing of the chamber signals is described in the following. Chamber signals are also used in the trigger.

Since the number of cells is a multiple of six for all layers, connections to the wires are in groups of six. Connection to six adjacent sense wires of the same layer are shown in fig. 14. In order to distribute the material of circuits and cables evenly over the end-plates, the high voltage and signal lines of different layers are connected alternately at either end. Fig. 15 shows a photograph of the six channel HV cards and preamps, which are mounted on the chamber end-plates.

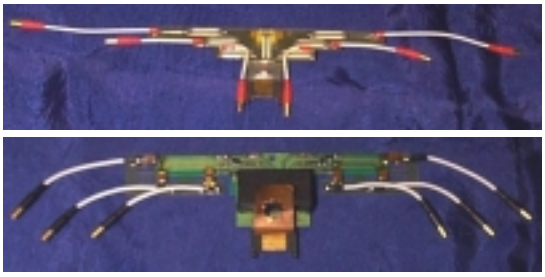

Figure 15: Photograph of the high voltage (top) and preamplifier boards (bottom).

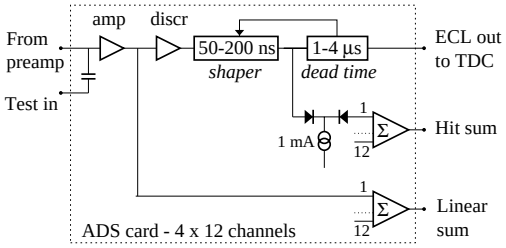

Figure 16: Block diagram of the off-chamber electronics.

The bulk of the ionization in the chamber is due to beam background and decreases with radius. For this reason, and for a uniform distribution of the cables, the number of sense wires connected to each HV line increases with the radius from a minimum of one 6-cell group for the inner layers to a maximum of six 6-cell groups for the outer ones. Each cable contains 24 HV lines; all wires are connected through 10 MΩ limiting resistors and decoupling between 6-channel cards is by means of a 1 MΩ - 470 pF filter. There are a total of 720 HV lines, each connected to an independently settable channel of 30 power supply modules (24 channels each, each module corresponding to a HV cable), housed in 3 crates.[6] Setting of the channels parameters is done serially via CaenNet by the slow control. The parameters are: high voltage settings, voltage ramp up and down speed, current and time over current. A continuous log of voltage, current and trip status has been kept by the slow control system since the beginning of operation of the experiment.

Details of the preamplifier are given in [28]. The measured preamplifier response is of order of 1.0 mV/fC. The sense wires have a capacitance of $\sim$ 30 pF, a resistance of $\sim$360 Ω and are not terminated on the HV side. The input network transfers about 1/3 of the charge to the preamplifier. With a gas gain of 10^5, the average output pulse height for a single electron cluster is $\sim$8 mV. The preamplifier output pulses are sent to an amplifier-discriminator-shaping circuit (ADS) via 50 Ω miniature coaxial cables, 15 m long. A cable bundle carries the signal coax, the low voltage supply and a line for injecting a test pulse.

A block diagram of the ADS board is shown in fig. 16. Boards are housed in 20 VME crates. Each crate has up to 16 ADS boards, the summing board for the first level trigger (SUPPLI, see below), and a control board for auxiliary services under KLOE slow control management[29]. An ADS board processes

[6] CAEN, Italy

48 chamber signals. Each channel consists of a $\times 12$ voltage amplifier and a discriminator with shaping circuits to set the output width, 50-250 ns, and dead time, 0.5-4 μs. Thresholds, width and dead time can be independently set for groups of 12 channels. Two additional outputs are provided for each group. The first is a linear sum of the input signal amplitudes for $\mathrm{d}E/\mathrm{d}x$ measurements. The second is an analog signal with discrete values proportional to the number of wires above threshold, used by the trigger[30]. The drift chamber trigger is based on the multiplicity and topology of wire signals. The SUPPLI board performs second-level summing-limiting, combining information from up to 8 groups of 12 contiguous wires. Each card has 8 such circuits.

Digitization of the drift time is performed by the chamber TDC's. A fully digital chip was developed for KLOE, using advanced 1/2 μ CMOS technology. [31] The 32 channel chip has a 1 GHz phase-locked clock, driving a free-running Grey-encoded counter. Upon arrival of a signal from the ADS discriminator, the count is transferred to a register. The chip can buffer 16 timing edges per event and 4 events per channel, with empty channel suppression read-out. It can operate in common start and common stop mode. In KLOE the TDC operates in common stop, the stop generating an additional counter value. We only use the earliest edge arrival minus the stop signal times. The chip however operates in multi-hit mode.

10 Test with Cosmic Rays

The drift chamber was tested with cosmic rays in the KLOE assembly hall before the detector was moved into DAΦNE hall. Data were taken both with and without magnetic field. The cosmic-ray trigger was from calorimeter information [30]. A software filter using calorimeter data was also used. The gas mixture was 89.4% helium and 10.6% isobutane. The gas flow rate was 30 slm corresponding to about one change of the volume per day.

Fig. 17 and 18 show the average of the efficiency over all layers for big and small cells for different values of the high voltage at fixed threshold and of the threshold at fixed high voltage (computed in the case of almost straight tracks). The values of the operating voltages chosen during data taking were 1950 V on the big cells and 1830 V on the small cells, with a threshold setting on ADS boards equivalent to 4 mV at the output of the preamplifier. In these conditions a single electron cluster provided a signal with an average pulse height of 10 mV, consistent with a gas multiplication factor of about 10^5.

11 Track reconstruction

The track reconstruction algorithms [33] are based on the program developed for the ARGUS drift chamber [34]. This program has been adapted to the all-stereo geometry and tuned to the specific topology of the events to optimize the efficiency of vertex finding over the whole volume of the drift chamber. The wire geometry, the space-time relations for each drift cell and the map of the magnetic field are described in detail in the program database. Event reconstruction is performed in three steps: i) pattern recognition, ii) track fit, and iii) vertex fit. Each step is handled separately and produces the information for the subsequent

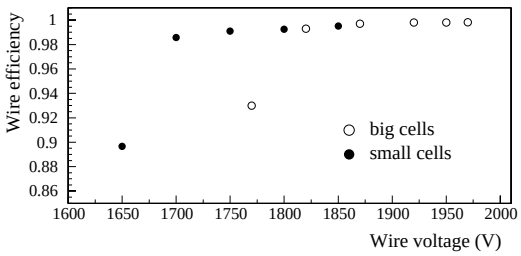

Figure 17: Efficiency for the big (open circle) and small cells (full circle) as a function of the HV settings, at a threshold of 4 mV.

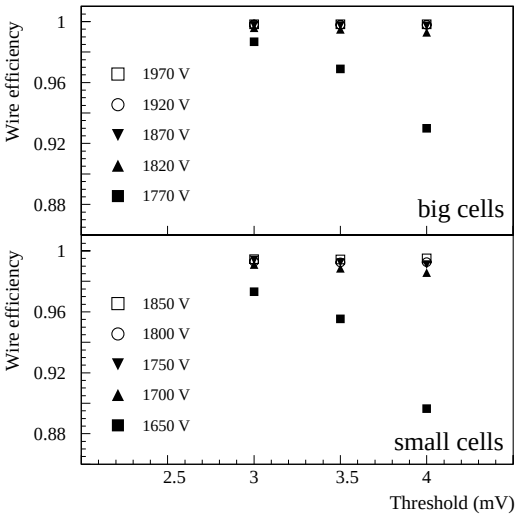

Figure 18: Efficiency for the big cells (top) and small cells (bottom) vs threshold and high voltage settings.

step.

11.1 Pattern recognition

In the following we shall call a 'hit' the presence of a wire signal and the relevant information. The pattern recognition algorithm begins by associating hits, working inward from the outermost layer. Track segments and approximate parameters of their trajectories are obtained. The input data are the drift distances and their errors as determined by the "raw" space-time relations (see sec. 11.4). Track segments are searched first in the transverse (x, y) plane; then the z coordinates are determined.

A track in the chamber is seen in the stereo views as two distinct images. For each stereo view, starting from the outermost layer, hits close in space are associated to form hit chains. When at least three hits are associated, hit $n + 1$ is added to the chain if the curvatures of the chains of hits $n - 2, n - 1, n$ and $n - 1, n, n + 1$ are consistent with each other. At the beginning all possible combinations due to the 'left-right' ambiguity are valid but a χ^2 estimator is computed for each combination. When chains of four hits are found, more hits are added, keeping only the combination with the lowest χ^2 value. At this stage, a hit can belong to different chains. A single view track candidate requires at least four hits in at least two wire layers.

At the end of the hit association each track candidate is refit and its parameters are computed. The track candidates from the two views are combined in pairs according to their curvature values and geometrical compatibility. The z coordinates are determined a this point from a three-dimensional fit to all associated hits.

11.2 Track fit

The track fit is obtained from minimizing the χ^2 function employing estimates of the hit resolutions. Since the space-time relations depend upon the track parameters, the final solution requires iteration. Recurrent relations (*tracing relations*) are used at each step to determine the positions of successive hits from the "raw" space-time relations and the track incidence angle; then the drift distance is corrected using the "fine" space-time relations. The residuals are then then determined and used for subsequent corrections to the "fine" space-time relations, (see sec. 11.4).

At each tracking step, the effects of energy loss and multiple scattering are estimated. The momentum loss between consecutive hits is computed assuming the pion mass. Multiple scattering is accounted for by dividing the track into segments whose length is chosen such that the transverse displacement expected due to the multiple scattering is smaller than the spatial resolution. The values of the effective scattering angles in the transverse and longitudinal plane are then treated as additional parameters in the track fit.

After the first iteration a number of procedures improve the quality of the track fit. In particular, dedicated algorithms are used to

- check the sign assignment of the drift distance hit by hit;

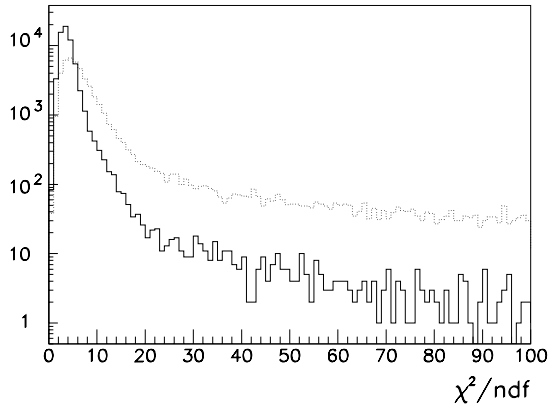

Figure 19: χ^2 distribution at the first iteration (dashed line) and at the end of the track fit (continuous line).

- add hits that were missed by the pattern recognition to the track;
- reject hits wrongly associated to the track by the pattern recognition;
- identify split tracks and join them.

Fig. 19 shows the distribution of χ^2/ndf at different stages of the track fit at the first iteration and after these refinements.

11.3 Vertex fit

The track parameters are used to search for primary and secondary vertices. For each track pair a χ^2 function is evaluated from the distances of closest approach between tracks and the extrapolation errors. The vertex position is determined by minimizing χ^2. To reduce the number of combinations, the tracks are first extrapolated to the beam-crossing point in the transverse plane and primary vertices are searched for using tracks with an impact parameter smaller than 10% of the radius of curvature. Secondary vertices are then searched for excluding tracks associated to another vertex. In the extrapolation, the track momentum is corrected for the energy loss in the beam pipe and in the drift chamber inner wall, and the effect of multiple scattering is taken into account in evaluating the covariance matrix. The pion mass is assumed when these corrections are evaluated.

11.4 Space-time relations

Several effects influence the dependence of the drift time on the distance from the wire. The drift velocity varies over a wide range as a function of the electric field and, due to the geometry of the drift cells, the electric field changes along the wire. These effects produce a dependence of the space-time (s–t) relations upon the orientation of the track and its position along the wire.

Simulation studies [35] have shown that the s–t relations in a single cell can be parametrized in terms of the dependence upon the angles β and $\tilde{\phi}$ as defined in fig. 20 with the β angle varying from $65^{\,o}$ to

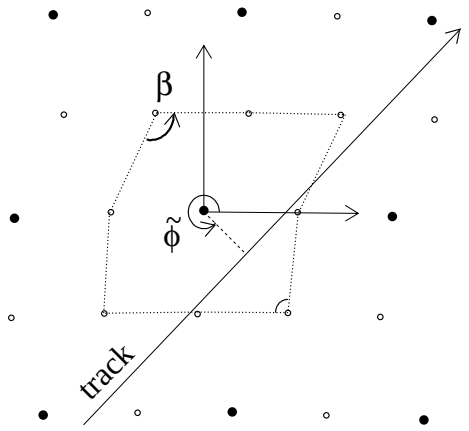

Figure 20: Definition of β and $\tilde{\phi}$, characterizing the shape of the cell and the angle of incidence of the track.

125^o. Six cells of different shape, chosen as "reference cells", are used to parametrize the s–t relations. In each of these reference cells the $\tilde{\phi}$ angle is divided into 36 intervals of 10^o. Since the deformation affects only the upper part of the drift cell in fig. 20, there are a total of $16 \times 6 + 20 = 116$ sets for the small cells and 116 sets for the big cells.

The s–t relations are determined using cosmic ray particles which ensure an almost uniform illumination over the whole chamber volume and cover the whole interval in the $\tilde{\phi}$ angle in each cell.

11.5 Calibration procedure

Cosmic ray particles are selected by an online filter which requires at least two calorimeter clusters well separated in space and a track candidate in the drift chamber with at least 40 cell signals. The contributions to the time measurement are expressed as

$$t = T_{tof} + T_{wire} + T_{drift} + T_o$$

where T_{tof} is the particle time of flight between the calorimeter and the wire, T_{wire} is the propagation time of the signal along the wire, T_{drift} is the drift time and T_o is a time offset. The first step of the calibration procedure is the determination of T_o. T_{tof} and T_{wire} are determined event by event with the information from the trigger and the calorimeter by approximating the track as a straight line. For each wire the $T_{drift} + T_o$ distribution (fig. 21) is fitted with the function

$$a + b\,\frac{e^{-d(t-T_1)}}{1+e^{-(t-T_o)/c}}$$

where a accounts for the contribution from accidentals and the fall is described by an exponential. T_o is defined by the point of maximum of the first derivative of the distribution and the parameter c gives an estimate of the time resolution close to the wire. The distribution of T_o for all wires is shown in fig. 22: the r.m.s. width of the distribution, $2.9\ ns$, represents the contribution to the time resolution due to the jitter of the wire signals and to the trigger.

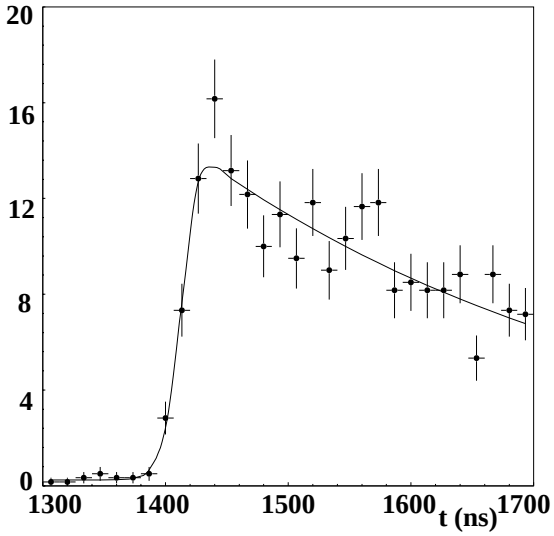

Figure 21: Example of time distribution fit for the determination of T_o (see text).

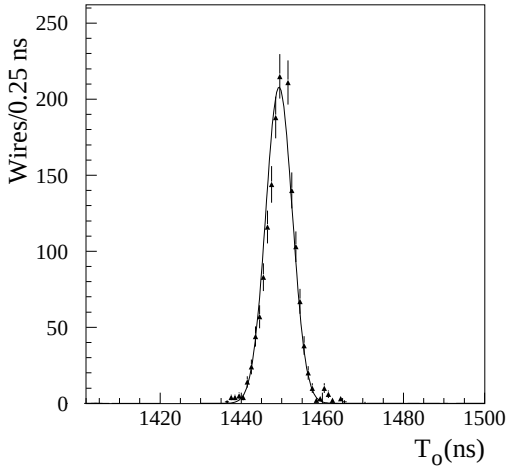

Figure 22: Distribution of T_o for all the wires connected to the same data acquisition chain.

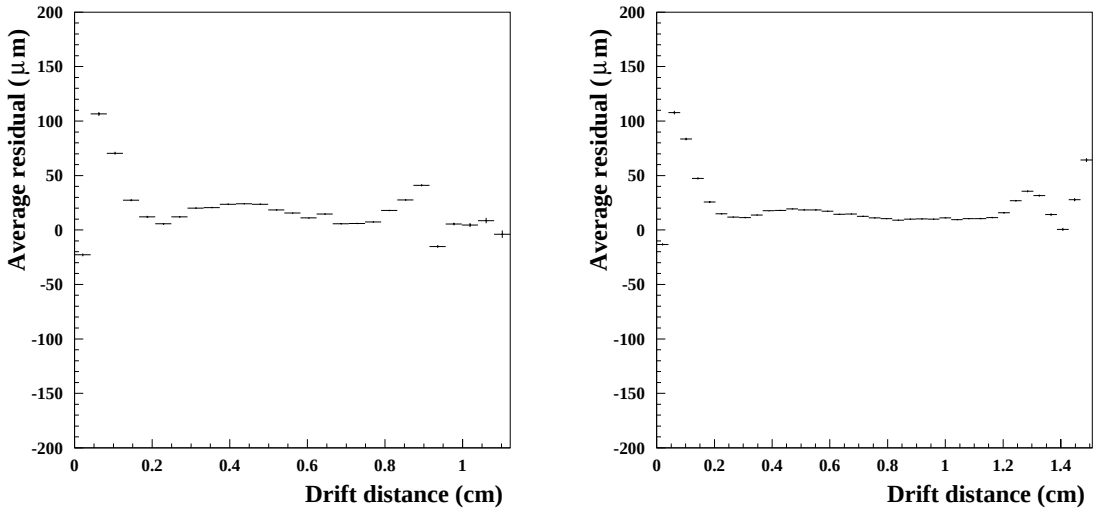

Figure 23: Mean values of the residuals at the end of the calibration procedure as a function of the drift distance for small (left) and big (right) cells for tracks with $\tilde{\phi} \sim 0$.

The s–t relation parameters are obtained using an iterative procedure [36]. The procedure was devloped using simulation studies and tested with data from the full-length chamber prototype [16]. The drift distance is parametrized in terms of a 5th order Chebychev polynomial [37], $d(C_k, t - T_o)$, where the C_k are 6×232 coefficients accounting for cell type (small or big), track orientation ($\tilde{\phi}$ angle), and cell shape (β angle). The input values of the C_k coefficients and of the resolution function $\sigma(d)$ are set equal to the mean values determined from the previous calibration run. Since before the track fit there is no information on the values of the $\tilde{\phi}$ and β parameters, the coefficients C_k^0 are averaged over all track orientations and drift cell shapes. The Chebychev polynomials with average coefficients are called "raw" space-time relations.

The drift distances $d_i(C_k^0)$ are used to fit the track and the residuals from the fit, $r_i = d_i^{fit} - d_i(C_k^0)$, are used to compute the track χ^2

$$\chi^2 = \sum_i \left(\frac{d_i^{fit} - d_i(C_k^0)}{\sigma(d_i)} \right)^2$$

Tracks with $\chi^2/\mathrm{dof} > 10$ are not used in the calibration procedure. The values of t_i, $d_i(C_k)$, d_i^{fit} are stored in a bank according to the values of the $\tilde{\phi}$ and β parameters defined by the track fit. The 232 residual distributions are then binned in intervals of drift distance of 300 μm width and fitted with Gaussians to determine the mean value $\langle r_j(C_k^0) \rangle$ and the variance in each bin. By an iterative procedure, the $d_i(C_k)$ are corrected by minimizing the absolute values of the residuals, $|r_i(C_k)|$, for each of the 232 distributions and then refitting the track. This iteration is halted when the mean value of the residual distribution $|\langle r(C_k) \rangle|$ is smaller than 100 μm.

Fig. 23 shows the distribution of the mean values of the residuals at the end of the calibration procedure as a function of the drift distance. As a final step the 232 "fine" space-time relations are fitted using the drift times and the corrected values of the drift distances and the final set of coefficients C_k is determined.

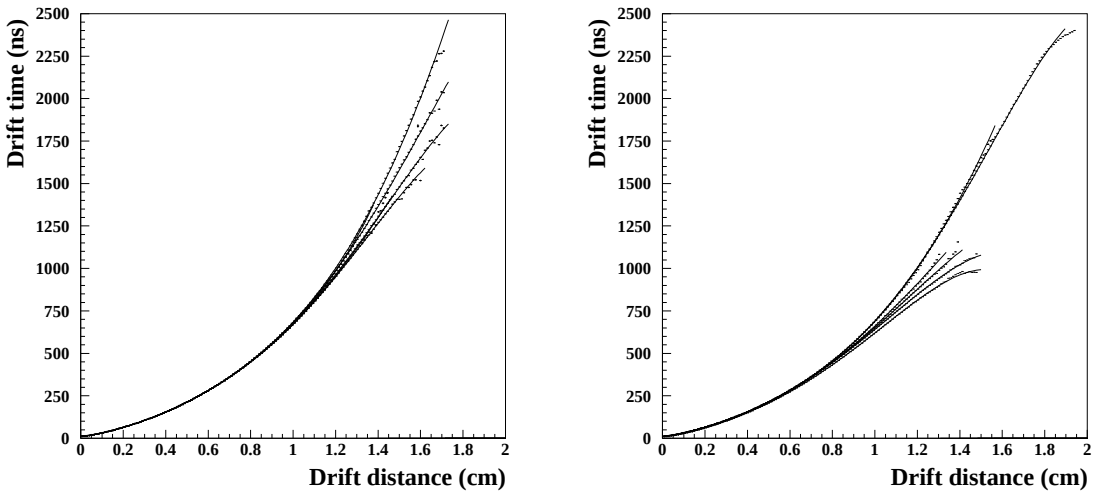

Figure 24: Time to space relations for the different values of the shape parameter β (left) and for different incidence angles $\tilde{\phi}$ (right).

Fig. 24 shows a set of s–t relations and their dependence upon the $\tilde{\phi}$ and β parameters.

The 200,000 tracks needed to fully calibrate the drift chamber are collected in three hours of data taking with colliding beams. Usually three iterations are sufficient to obtain a new set of calibration parameters.

11.6 Spatial resolution

The spatial resolution versus drift distance is shown in fig. 25, averaged over all small and all big cells for a single $\tilde{\phi}$ value. The spatial resolution averaged over the whole detector is smaller than 200 μm for a large part of the drift cell and is almost independent of the track direction and cell shape.

The different contributions to the resolution function have been studied: primary ionization statistics, longitudinal electron diffusion and the jitter in the time measurement. Fig. 26 shows a fit of the spatial resolution for the big cells. The range of the drift distance is limited to values less than 1.1 cm to avoid the region where irregularities of the field lines introduce large distortions. The contribution from primary ionization statistics has been parametrized as a function of λ, the mean path between two consecutive ionizing collisions. The best fit gives $\lambda = 770 \pm 14$ μm corresponding to $n_p = 13.0 \pm 0.2$ clusters/cm. The contribution due to electron diffusion has been parametrized as the product of a term which depends on the number of clusters corresponding to the arrival of the first electron, n_f, times the ratio of the diffusion coefficient and the drift velocity $D(E)/w(E)$ [38]. The best fit to the resolution function gives $n_f = 10.2 \pm 1.7$, using $D(E)/w(E) = (2.97 \pm 0.21)10^{-4}$ cm at a magnetic field of 0.6 T [9]. We determine a value for the contribution for diffusion of $\simeq 140\mu$m for 1 cm of drift. The above values are in good agreement with the results in tab. 2. The contribution due to the time resolution is convoluted with the s–t relations in fig. 24. The fit to the curve gives a resolution $\sigma_t = 4.4 \pm 0.2$ ns.

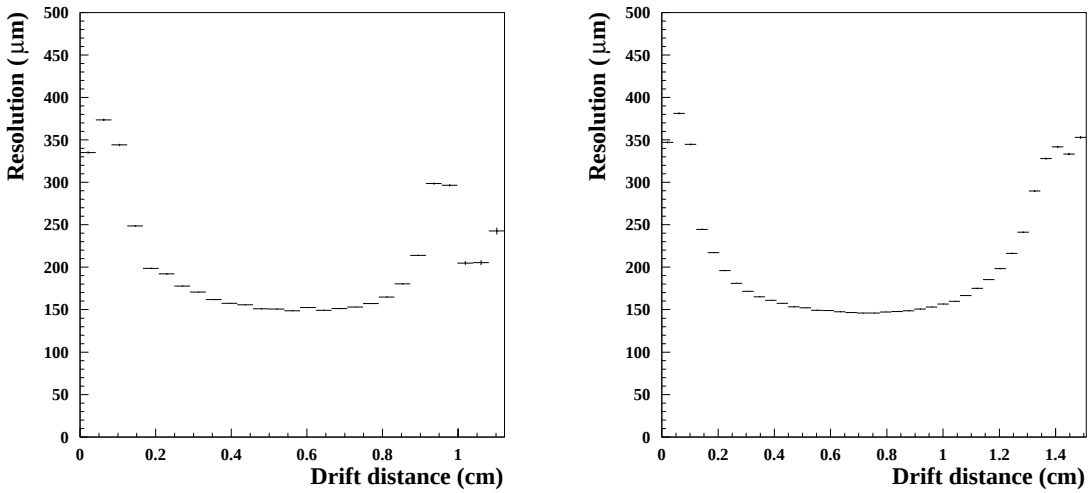

Figure 25: Spatial resolution for small (left) and big (right) cells, for tracks with $\tilde{\phi}\sim 0$.

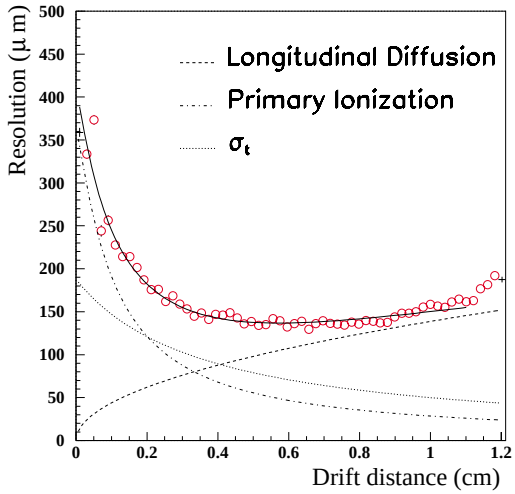

Figure 26: Average spatial resolution for big cells. The fit accounts for: electron longitudinal diffusion, primary ionization statistics, resolution of the time measurement σ_t.

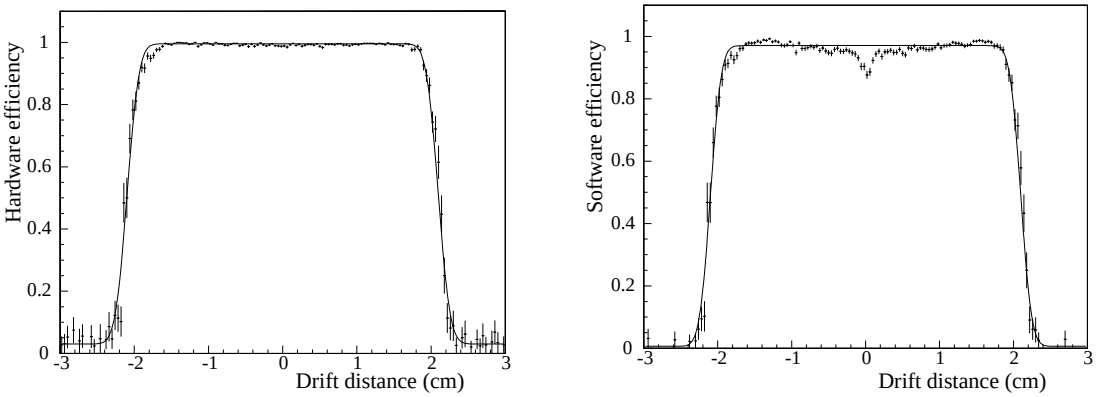

Figure 27: Hardware and software efficiency as a function of the drift distance.

11.7 Efficiency

Hits extrapolated from these tracks to different cells have been considered, without performing any cell by cell correction, in order to compute an average efficiency, which is shown in fig. 27 as a function of the drift distance.

The cell efficiency is determined using cosmic ray tracks with more than 96 hits and a χ^2/dof less than 5. The "hardware efficiency" is defined as the ratio of the number of hits found in a cell to the number of tracks crossing it. This efficiency is $\sim$99.6% both for big and small cells and is constant over the whole chamber volume. The "software efficiency" is defined by requiring the hit found in the cell to be used by the track fit, and was found to be 97%. As shown in fig. 27, the software efficiency is lower for small drift distances. This is related to the worse resolution close to the wire and to incorrect resolutions of the sign ambiguity by the pattern recognition algorithm.

12 Operation with colliding beams

In 1999 KLOE collected data with collisions in DAΦNE, for a total integrated luminosity of $\sim$2 pb $^{-1}$ with the magnetic field set at 0.56 T. Typically, DAΦNE ran with 300 mA currents, beam lifetimes of about 30 minutes and, at year end, a peak luminosity of $\sim 3 \times 10^{30}$ cm^{-2} s^{-1}.

At that time 60 out of 12,582 cells were not operating. The chamber operation was monitored using drift time distributions, the values of the space-time relations parameters and the track reconstruction efficiency. More refined checks to evaluate the vertexing and momentum resolution employed samples of Bhabha scattering events and $\phi \to K^+K^-$, $\to K_S K_L$ decays selected online.

The momentum resolution for 510 MeV/c electrons and positrons is shown in fig. 28 as a function of the polar angle. In the range $130^\circ > \theta > 50^\circ$, where the projected track length is constant, the resolution is 1.3 MeV/c. In a typical fill, with 10,000 Bhabha scattering events we measured the beam energy with an accuracy of 20 keV and the position of the luminous region with an accuracy of 0.05 mm in the vertical direction, y, where the beam profile is known to be about 20 μm. The distributions in the horizontal, x,

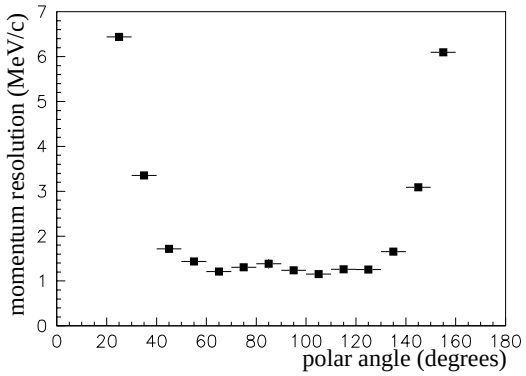

Figure 28: Momentum resolution for 510 MeV/c electrons and positrons as a function of the polar angle.

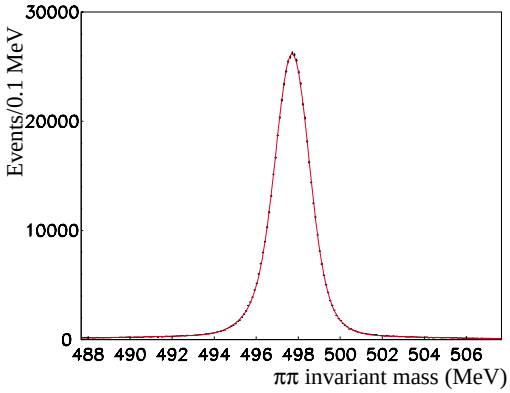

Figure 29: $\pi^+\pi^-$ invariant mass for verticies", with two unlike sign tracks.

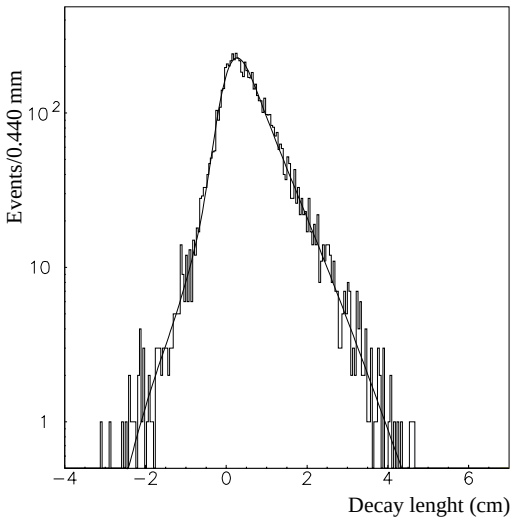

Figure 30: Decay length in the ϕ reference system for $K_S \to \pi^+\pi^-$ events. The data are fitted with an exponential convoluted with two Gaussians.

and longitudinal, z, projections determine the beam-beam interaction region widths of 1.2 mm and 12 mm respectively, with an accuracy of 0.05 mm in x and 0.1 mm in z.

The invariant mass reconstructed with two unlike sign tracks that form a vertex within 6 cm from the center of the luminous region, shown in fig. 29, clearly identifies $K_S \to \pi^+\pi^-$ decays. The distribution peaks at the correct value for the mass with a r.m.s. width of 0.9 MeV/c^2. The distribution of the decay length in the ϕ-system, shown in fig. 30 fitted with an exponential and two gaussians, reproduces the value of the lifetime of 110 MeV/c K_S consistent with a resolution for secondary vertices better than 3 mm.

Looking for additional vertices associated to $K_S \to \pi^+\pi^-$ decays, we clearly identify K_L decays into charged particle pairs. The distribution of the K_L decay path shows that the efficiency for detecting secondary vertices is constant in the volume of the drift chamber up to $r \simeq 150$ cm and gives the correct value for the K_L decay length. For charged particle pairs with no missing momentum, the $\pi^+\pi^-$ invariant mass distribution shows a clear peak at the K_L mass with a resolution of 1.0 MeV/c^2, indicating that the CP–symmetry violating decay is identified with negligible background. In case of missing momentum, the missing mass distribution, computed with the correct mass hypothesis, is peaked at zero for $K_L \to \pi e\nu$ and $K_L \to \pi\mu\nu$ decays and at the neutral pion mass for $K_L \to \pi^+\pi^-\pi^0$ decays. Figure 31 shows the missing mass distribution for secondary vertices associated to $K_S \to \pi^+\pi^-$ decays assuming the pion mass hypothesis for both tracks. The π^0 mass is reconstructed with a resolution of 1.2 MeV/c^2.

13 Conclusions

The KLOE drift chamber is one of the largest tracking detectors ever built. The performance specifications for its use in a low energy e^+e^- factory are very demanding to guarantee good momentum resolution for low momentum particles and low absorption of photons. The requirement of high trasparency poses severe

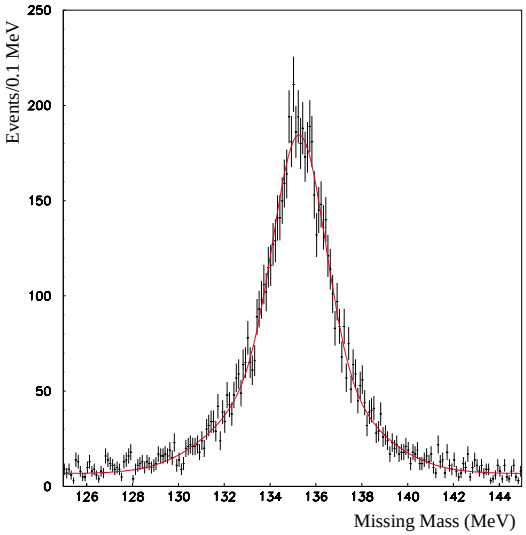

Figure 31: Missing mass distribution for K_L decays associated to identified K_S decays.

constraints on the choice of materials and the thickness of the chamber walls. The use of a low-density, high ionization potential gas is highly demanding for the front–end electronics. The whole mechanical structure is built with carbon fiber and the chamber volume is filled with a light gas mixture composed primarily of Helium. Many innovative techniques have ben devised for the construction of the mechanical structure and the stringing of the wires.

An important feature of the detector is the ability to reconstruct secondary vertices over most of its active volume. For this purpose, an original arrangement of almost square drift cells in a "all-stereo" geometry has been adopted. Pattern recognition and track fitting algorithms have been developed for this wire configuration and optimized for finding secondary vertices. A procedure for self calibrating the highly non linear time-to-space relations of the drift cells has been implemented. Using cosmic ray tracks this procedure converges rapidly and provides the response and resolution functions for all drift cells. A spatial resolution better than 200 μm is obtaneid.

The detector, after a debugging period with cosmic rays, was operated for several months during the commissioning of the DAΦNE rings. The preliminary results of the data analysis show that the drift chamber meets the design specifications well.

Acknowledgements

We want to warmly acknowledge the continuous support of INFN.

We deeply thank the contribution of LNF technicians in the construction and in the operation of the KLOE drift chamber:

- the LNF-Electronic and Automation service: U. Denni and M. A. Frani for the design, the construction and the test of the automated wiring system and of the gas system; G. Papalino, R. Lenci,

M. Santoni, D. Riondino, F. Bertino for the realization, test and installation of readout electronics;

- M. Anelli for the installation of the chamber and the maintenance of the gas system;
- M. Carletti for the realization of the control systems;
- A. Rutili and the LNF-SSCR service: G. Bisogni, G. Ferretti, A. De Paolis, G. Ferretti, E. Iacuessa, U. Martini, L. Iannotti, A. Ceccarelli, A. Di Virgilio, G. Catitti, B. Ortensi, A. Tiburzi, for the toolings, the assembly, the construction and the survey of the chamber;

We acknowledge the mechanical and electronic services of the Sezione INFN and Physics Departments of Lecce:

- C. Pinto and R. Assiro for the design and construction of the electronics both for the stringing robots and the ADS boards;
- G. Fiore for the realization of the stringing robots mechanics.

The design, construction and installation of the detector was possible thanks to the skill of the mechanical support of the Sezione INFN and Physics Departments of Roma ”La Sapienza” and Roma ”Tor Vergata”: We warmly thank

- F. Bronzini, A. Pelosi and S. Casani for the design of the stringing support;
- A. Olivieri for the construction of the stringing robotics and the assembly of the drift chamber;
- M. Gatta, E. Gennari and A. Rossi for the design, realization, test and installation of readout electronics.

Finally we have to acknowlegde the help of the Physics Department of Karlsruhe University:

- K. Kärcher for the design and maintenance of the gas circulating system;

Work partially supported by German Ministry of Education and Research (BMBF) under contracts (06 KA 654 TP3), (06 KA 564 TP2), (06 KA 860), (06 KA 957);
Work partially supported by Graduiertenkolleg ’Elementarteilchenphysik an Beschleunigern’;
Deutsche Forschungsgemeinschaft;
Work partially supported by EURODAPHNE network, contract No. FMRX-CT98-0169;
Work partially supported by INTAS contracts No. (96-624) and (99-37);
Work partially supported by TARI contract HPRI-CT-1999-00088.

References

KLOE notes are available at **http://www.lnf.infn.it/kloe/pub/**

[1] The KLOE Collaboration, *The KLOE Detector Technical Proposal*, LNF-93/002, (1993); S.Bertolucci for the KLOE Collaboration, *A status report of KLOE at DAΦNE*, Proceedings of the 19th International Symposium on Lepton and Photon Interactions at High Energies, Stanford, USA (1999), hep-ex/0002030.

[2] The DAΦNE Project Team, *Proposal for a ϕ-factory*, LNF-90/031 1990; C.Milardi *et al.*, *Status of DAΦNE*, Proceedings of the Workshop on Physics and Detectors for DAFNE, Frascati, Italy (1999).

[3] L. Maiani, *CP and CPT violation in neutral kaon decays*, The Second DAΦNE Physics Handbook, Edited L.Maiani, G.Pancheri and N.Paver, INFN LNF (1995) 3.

[4] F.Cervelli *et al.*, Proceedings of the 1998 ICHEPC, Vancouver, Canada (1998); A.Di Domenico *et al.*, Proceedings of the VIII ICCHEP, Lisbon, Portugal (1999); E.Santovetti *et al.*, Nucl. Phys. Proc. Suppl. **78** (1999) 157.

[5] The KLOE Collaboration, *The KLOE Central Drift Chamber* LNF-94/028, (1994); G. Bencivenni *et al.*, *Nucl. Instrum. Meth.* **A419** (1998) 320.

[6] G.Finocchiaro, F.Grancagnolo and S.Spagnolo, *Cell geometry of the KLOE drift chamber*, KLOE *note* **157** (1996).

[7] GARFIELD, CERN program library, entry W5050.

[8] G.Finocchiaro *et al.*, *Nucl. Instrum. Meth.* **A360** (1995) 48.

[9] C.Avanzini *et al. Nucl. Instrum. Meth.* **A449** (2000), 237.

[10] G.Bencivenni *et al.*, *The prototype 0 of the KLOE tracking chamber*, KLOE *note* **79** (1993).

[11] P.Bernardini *et al.*, *Nucl. Instrum. Meth.* **A355** (1995) 428.

[12] C.Grab, ETHZ IMP PR92-5; G.Cataldi *et al.*, *Nucl. Instrum. Meth.* **A386** (1997) 458.

[13] V.Golovatyuk, F.Grancagnolo and M.Primavera, *Nucl. Instrum. Meth.* **A394** (1997) 97;

[14] A.Sharma and F.Sauli, *Nucl. Instrum. Meth.* **A350** (1994) 470.

[15] S.F.Biagi, *Nucl. Instrum. Meth.* **A283** (1989) 716.

[16] A.Andryakov *et al.*, *Nucl. Instrum. Meth.* **A404** (1998) 248.

[17] S.Moccia, *Design of the KLOE drift chamber endplates*, KLOE *note* **169** (1998).

[18] D.G.Cassel *et al.*, *Nucl. Instrum. Meth.* **A252** (1986) 325.

[19] P.Giubellino *et al.*, *Nucl. Instrum. Meth.* **A252** (1986) 528; R.Bouclier *et al.*, CERN-PPE, 95-36 (1995).

[20] G.Bencivenni *et al.*, *Ageing test of the KLOE drift chamber wires*, KLOE *note* **143** (1995).

[21] G.Bencivenni *et al.*, *Creep measurement on Al-5056 wires*, KLOE *memo* **138** (1997), unpublished.

[22] G.Bencivenni *et al.*, *An Automated Facility for Stringing the KLOE Chamber*, KLOE *note* **149** (1995).

[23] G.Bencivenni *et al.*, *Equipment and procedure for stringing the KLOE Drift Chamber*, KLOE *note* **171** (1998).

[24] S.Dell'Agnello *et al.*, *Survey and alignment of the KLOE experiment at DAFNE*, LNF-97/045 (1997); S.Dell'Agnello *et al.*, Nucl. Phys. **B 54B** (1997) 57.

[25] A. Andryakov *et al.*, *Nucl. Instrum. Meth.* **A409** (1998) 63.

[26] U.von Hagel, A.Denig, W.Kluge, F.Schönleber, *Nucl. Instrum. Meth.* **A 420** (1998) 429.

[27] The KLOE Collaboration, *The KLOE Data Acquisition System*, LNF-94/028, (1994).

[28] R.J.Yarema *et al.*, *IEEE Transactions on Nuclear Science*, 39 (1992) 742.

[29] A.Cardini *et al.*, *The KLOE Slow Control System*, KLOE *memo* **206** (2000), unpublished.

[30] The KLOE Collaboration, *The KLOE Trigger System*, LNF-96/043, (1996); V. Bocci *et al.*, *Trigger implementation in the KLOE experiments*, Proceedings of the 5th Conference on Electronics for LHC experiments, CERN-99-09 (1999) 281.

[31] M.Passaseo, E.Petrolo and S.Veneziano, *Nucl. Instrum. Meth.* **A367** (1995) 418; S. Veneziano, *Nucl. Instrum. Meth.* **A409** (1998) 363.

[32] The KLOE Collaboration: *The KLOE Data Acquisition System*, LNF-95/014, (1995); E.Graziani *et al.*, Proceedings of the International Europhysics Conference on High Energy Physics (1999), Tampere, Finland; The KLOE Collaboration: *Novel DAQ and Trigger methods for the KLOE Experiment*, Proceedings of the 30th ICHEP 2000, Osaka, Japan, hep-ex/0006039

[33] A.Antonelli *et al.*, *A short description of the track reconstruction program with the KLOE drift chamber*, KLOE *note* **157** (1996).

[34] K.W.Edwards *et al.*, *The Argus Vertex Drift Chamber*, *Nucl. Instrum. Meth.* **A252** (1986) 384.

[35] P.De Simone, *Cell response parametrization*, KLOE *note* **98** (1994).

[36] G.Cabibbo, P.De Simone, A.Ferrari, L.Pontecorvo and T.Spadaro, *The calibration of the space-time relations of the KLOE drift chamber*, KLOE *note* **175** (2001).

[37] M.Primavera and S.Spagnolo, *Parametrization of the time to distance relations and resolution in the KLOE drift chamber*, KLOE *note* **165** (1997).

[38] V.Palladino and B.Sadoulet, *Nucl. Instrum. Meth.* **175** (1975) 323.